January 1, 2007

Stability and Transient Dynamics of Thin Liquid Films Flowing over Locally Heated Surfaces

N Tiwari
Z Mester
JM Davis

Stability and transient dynamics of thin liquid films flowing over locally heated surfaces

Naveen Tiwari, Zoltan Mester, and Jeffrey M. Davis*
Department of Chemical Engineering, University of Massachusetts, Amherst, Massachusetts 01003, USA
(Received 25 June 2007; published 9 November 2007)

The dynamics and linear stability of a liquid film flowing over a locally heated surface are studied using a long-wave lubrication analysis. The temperature gradient at the leading edge of the heater induces a gradient in surface tension that opposes the gravitationally driven flow and leads to the formation of a pronounced capillary ridge. The resulting free-surface shapes are computed, and their stability to spanwise perturbations is analyzed for a range of Marangoni numbers, substrate inclination angles, and temperature profiles. Instability is predicted above a critical Marangoni number for a finite band of wave numbers separated from zero, which is consistent with published results from experiment and direct numerical simulation. An energy analysis is used to gain insight into the effect of inclination angle on the instability. Because the spatial nonuniformity of the base state gives rise to nonnormal linearized operators that govern the evolution of perturbations, a nonmodal, transient analysis is used to determine the maximum amplification of small perturbations to the film. The structure of optimal perturbations of different wave numbers is computed to elucidate the regions of the film that are most sensitive to perturbations, which provides insight into ways to stabilize the flow. The results of this analysis are contrasted to those for noninertial coating flows over substrates with topographical features, which exhibit similar capillary ridges but are strongly stable to perturbations.

DOI: 10.1103/PhysRevE.76.056306 PACS number(s): 47.15.gm, 47.20.Dr, 47.55.dm, 47.55.nb

I. INTRODUCTION

Many industrial and technological applications involve thin liquid films on heated surfaces [1,2], including coating and microfabrication processes [3,4], microelectromechanical systems (MEMS) [5], and microfluidic devices in which applied temperature gradients are used to control liquid motion [6,7]. Because surface tension is a function of temperature [8], the presence of a temperature gradient at the free surface results in a surface tension gradient, or Marangoni stress. Such stresses can cause thermocapillary flows and interfacial instabilities [9,10], which have been studied extensively for uniformly heated surfaces [11]. Much theoretical work has also been focused on the effect of surface tension gradients on the evolution of free-surface flows of thin liquid films [2,12,13], such as the long-wave instability for a liquid film flowing down a uniformly heated plane [14], rivulet formation [15], and related work that extends these analyses [16–19].

Thin films flowing over locally heated surfaces have also been studied recently. Kabov [20,21] performed experimental and theoretical investigations of the regular, spanwise rivulets that form due to hydrodynamic instabilities in films falling down an inclined plane containing a rectangular heater. It was shown that if the temperature increase at the heater is sufficiently small, a stable, two-dimensional flow with a capillary ridge, or "bump," at the leading edge of the heater is observed. As the heating increases the capillary ridge increases in size, and instability develops in the form of an array of longitudinal rivulets with a well-defined wavelength. The instability can ultimately lead to film rupture and dryout, which may restrict the use of liquid films on such heated surfaces.

In a subsequent study, Frank and Kabov [22] measured the temperature distribution at the free surface and studied the effect of the Reynolds, Prandtl, Weber, and Biot numbers on the critical Marangoni number (M_{crit}) at instability onset. They also used direct numerical simulation to solve the coupled three-dimensional energy and Navier-Stokes equations. Above M_{crit} the flow was found to be unstable for a band of wave numbers separated from zero. This work demonstrated that the rivulet instability occurs even for a Biot number of zero and is thus distinct from the thermocapillary instability of a film flowing over a uniformly heated plate [15]. Similarities were found with the fingering instability in a gravitationally driven fluid sheet spreading down an inclined plane [23], which warrants further investigation.

There are two published theoretical studies of this instability [24,25], but there are discrepancies of uncertain origin in the results [22]. Skotheim *et al.* [24] performed a lubrication analysis of a film flowing over a surface with periodic temperature increases (used to represent an infinite array of heaters). Convection terms were neglected in the momentum and energy equations. They predicted a long-wave instability, i.e., instability for wave numbers in an interval $(0, q_1)$. The flow was always unstable, but a critical Marangoni number was found for the onset of instability by extrapolating the heater periodicity to infinity. The predicted wavelength of the instability was within 20% of experiment, but the critical Marangoni number was about five times too large.

Kalliadasis *et al.* [25] studied the stability of a film flowing over a surface with a Gaussian temperature profile using an integral-boundary-layer approximation of the Navier-Stokes and energy equations for long waves, which retained the convective terms in the energy equation. A linear stability analysis revealed the existence of both a discrete and a continuous spectrum. The continuous spectrum was always stable, but the discrete spectrum was unstable beyond a critical Marangoni number for a band of wave numbers in the

*jmdavis@ecs.umass.edu

interval (q_1, q_2), with $q_1 > 0$. The reason for these differences in the qualitative nature of the instability [24,25] may be due to the temperature profile, boundary conditions, or neglect of the convective terms and requires further investigation.

In this work, a lubrication-based model is developed for a liquid film flowing over a locally heated surface. The capillary ridge that forms in response to the gradient in surface tension at the upstream edge of the heater is reminiscent of ridges that form in response to topographical variations of the isothermal substrate in noninertial coating flows [26,27]. In addition to exploring the differences between the predictions of Skotheim *et al.* [24] and Kalliadasis *et al.* [25], it is therefore of interest to study the stability characteristics, structure, and transient response of perturbations and compare with results for topographical features. Furthermore, the influence of substrate inclination angle, which can add a hydrostatic component to the pressure in the film, is assessed through stability and energy analyses and compared to experimental results. Like noninertial flow over topographical features, a stable, continuous spectrum is found that corresponds to decaying capillary waves whose shape is modified by the fluid ridge that forms due to the Marangoni flow induced by the heater. Similarly, stable, discrete modes are also found for perturbations of large wave numbers. For sufficiently large Marangoni numbers, however, an unstable band of discrete modes is found for a finite band of wave numbers separated from zero, which corresponds to the rivulet formation observed experimentally. The use of appropriate dimensionless variables recovers the experimental dependence of the instability wavelength on the surface tension and reveals the similarities with fingering instabilities in a spreading fluid sheet [23,28].

In Sec. II, a mathematical model is derived by reducing the Navier-Stokes and energy equations using a long-wave lubrication approximation. In Sec. III A, base profiles are shown for various temperature profiles at the solid substrate. The streamlines of the flow are presented in Sec. III B and compared to those in other flows of thin films that exhibit capillary ridges. Results from a linear stability analysis are presented in Sec. IV A, including the influence of the temperature profile and substrate inclination angle. Because the spatial nonuniformity of the base state gives rise to nonnormal linearized operators, a nonmodal, transient analysis is used to determine the maximum amplification of small perturbations to the film. Results for the amplification ratio and structure of optimal perturbations of different wave numbers are presented in Secs. IV B and IV C. In Sec. IV D, an energy analysis is performed to explore the effect of the inclination angle of the substrate on the linear stability of the base profiles. A comparison of the results to experiment and related instabilities is presented in Sec. V. Conclusions are presented in Sec. VI.

II. MATHEMATICAL MODEL

Consider a liquid film flowing down a plane that is inclined at an angle θ to the horizontal, as shown in Fig. 1. A heater is embedded in the substrate and produces the temperature field $\hat{T}_0(x)$ at the plate surface, and the thickness of

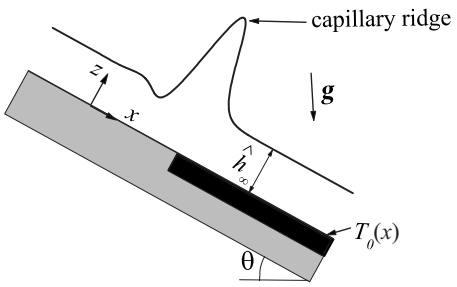

FIG. 1. Schematic diagram of a thin liquid film flowing over a heater. The Marangoni stress at the edge of the heater opposes the gravitational flow, which leads to the formation of a capillary ridge.

the film far away from the heater is uniform at $\hat{h}_\infty$. The coordinate system is constructed with $\hat{x}$ in the direction of flow and $\hat{z}$ normal to the substrate. The velocity $(\hat{\boldsymbol{u}})$, pressure $(\hat{p})$, and temperature $(\hat{T})$ fields are governed by the Navier-Stokes equation

$$\hat{\boldsymbol{u}} \cdot \hat{\boldsymbol{\nabla}} \hat{\boldsymbol{u}} = \frac{-1}{\rho} \hat{\boldsymbol{\nabla}} \hat{p} + \nu \hat{\boldsymbol{\nabla}}^2 \hat{\boldsymbol{u}} + \boldsymbol{g}, \tag{1}$$

the continuity equation for an incompressible fluid,

$$\hat{\boldsymbol{\nabla}} \cdot \hat{\boldsymbol{u}} = 0, \tag{2}$$

and the energy equation,

$$\hat{T}_t + \hat{\boldsymbol{u}} \cdot \hat{\boldsymbol{\nabla}} \hat{T} = \alpha_{th} \hat{\boldsymbol{\nabla}}^2 \hat{T}, \tag{3}$$

where ν is the kinematic viscosity, ρ is the fluid density, and α_{th} is the thermal diffusivity. Dimensional variables are denoted with a hat symbol $(\hat{\cdot})$.

At the plate surface, the no-slip and no-penetration boundary conditions are enforced,

$$\hat{\boldsymbol{u}}(\hat{z} = 0) = \boldsymbol{0}. \tag{4}$$

The normal and tangential stress balances at the free surface $[\hat{z} = \hat{h}(\hat{x}, \hat{y}, \hat{t})]$ are

$$\boldsymbol{n} \cdot \hat{\boldsymbol{\Gamma}} \cdot \boldsymbol{n} = \gamma (\hat{\boldsymbol{\nabla}}_s \cdot \boldsymbol{n}), \tag{5}$$

$$\boldsymbol{t} \cdot \hat{\boldsymbol{\Gamma}} \cdot \boldsymbol{n} = -\boldsymbol{t} \cdot \hat{\boldsymbol{\nabla}}_s (\gamma), \tag{6}$$

where $\hat{\boldsymbol{\Gamma}} \equiv \mu [\hat{\boldsymbol{\nabla}} \hat{\boldsymbol{u}} + (\hat{\boldsymbol{\nabla}} \hat{\boldsymbol{u}})^t]$ is the viscous stress tensor for a Newtonian fluid of viscosity μ and γ is the liquid-gas surface tension. The heater is assumed to be a good conductor of heat,

$$\hat{T}(\hat{x}, \hat{y}, \hat{z} = 0) = \hat{T}_0(\hat{x}). \tag{7}$$

Balancing conduction through the film with convective heat transfer to the surrounding gas at $\hat{z} = \hat{h}$ yields

$$-k_{th} \boldsymbol{n} \cdot \hat{\boldsymbol{\nabla}} \hat{T}^i = H(\hat{T}^i - \hat{T}_\infty), \tag{8}$$

where k_{th} is the thermal conductivity of the liquid and H is the film heat transfer coefficient at the liquid-air interface. The temperature field at the liquid-air interface is

$\hat{T}^i \equiv \hat{T}(\hat{z}=\hat{h})$, and $\hat{T}_\infty$ is the temperature of the air and liquid far away from the heater.

Equations (1)–(8) are reduced to a tractable model by introducing appropriate dimensionless variables. In the $\hat{z}$ direction, the constant film thickness away from the heater $\hat{h}_\infty$ is the appropriate length scale. In the streamwise and spanwise directions, the dynamic capillary length, $l_c=\hat{h}_\infty(3\mathrm{Ca})^{-1/3}$, is used as the length scale, where $\mathrm{Ca}=\mu U_c/\gamma_0$ is the capillary number. This choice of a flow-dependent length scale based on the balance of viscous and capillary forces (vs a characteristic length of the temperature gradient) has the advantage of placing a parameter in the boundary conditions (temperature profile) rather than in the governing partial differential equation, which is analogous to the case of a thin liquid film flowing over an isothermal substrate bearing topographical features [29]. Here, $\gamma_0 \equiv \gamma(\hat{T}=\hat{T}_\infty)$ is the surface tension at the reference temperature $\hat{T}_\infty$. The pertinent velocity scale in the streamwise direction is $U=\rho g \hat{h}_\infty^2 \sin\theta/(3\mu)$, which is obtained by balancing viscous effects and gravity. This velocity scale should be used in Ca to determine the length scale l_c used in the small lubrication parameter $\hat{h}_\infty/l_c$. In what follows, however, the velocity scale is chosen to be $U_c=\rho g \hat{h}_\infty^2/(3\mu)$. While strictly appropriate only for a vertical substrate, this choice of velocity scale makes the length l_c independent of inclination angle and therefore ensures that the same temperature profile exists at the solid surface as θ varies, which allows the effect of inclination angle on the film profile and stability to be isolated. The dimensionless coordinates are thus $x=\hat{x}/l_c$, $y=\hat{y}/l_c$, and $z=\hat{z}/\hat{h}_\infty$. This analysis would also apply to the spin coating of liquid films over differentially heated surfaces, with the body force term and velocity scale changed accordingly [27].

Introducing these scalings, Eq. (1) reduces at leading order to

$$u_{zz} = P_x - 3, \tag{9}$$

$$v_{zz} = P_y, \tag{10}$$

and

$$P_z = -3\mathrm{G}\cos\theta, \tag{11}$$

where (u,v,w) are the dimensionless components of velocity in the (x,y,z) directions, respectively. The dimensionless group that characterizes the influence of hydrostatic pressure is $\mathrm{G}\cos\theta=(3\mu U_c/\gamma_0)^{1/3}\cos\theta$. Note that with the choice of U_c as the characteristic velocity scale used to write the dimensionless equations (as opposed to U in the application of the lubrication approximation to simplify the equations), G can be $O(1)$ for very small θ even if $\mathrm{Ca}_0^{1/3} \equiv (\mu U/\gamma_0)^{1/3}$ is small. This simplification of the Navier-Stokes equation requires $\mathrm{ReCa}_0^{1/3} \ll 1$, where $\mathrm{Re}=U\hat{h}_\infty/\nu$, and $\mathrm{Ca}_0^{2/3} \ll 1$.

At leading order, the boundary conditions in Eqs. (4)–(6) simplify to

$$\boldsymbol{u}(z=0) = \mathbf{0}, \tag{12}$$

$$P(z=h) = -\nabla^2 h, \tag{13}$$

and

$$\partial \boldsymbol{u}/\partial z(z=h) = -2\mathrm{M}\nabla T^i, \tag{14}$$

where $\mathrm{M}=3^{1/3}\gamma_T \triangle T/(2\gamma_0 \mathrm{Ca}_0^{2/3})$ is the Marangoni parameter and T^i is the dimensionless temperature field at the interface that is found from the energy equations. Again $\mathrm{Ca}_0^{2/3} \ll 1$ is assumed in these equations. Beginning with Eq. (13), $\boldsymbol{\nabla}$ and $\boldsymbol{u}$ represent the x and y components of the dimensionless gradient operator and velocity field, respectively, for the remainder of this paper. In Eq. (14) a linear variation of surface tension with temperature is assumed, $\gamma(\hat{T})=\gamma_0-\gamma_T(\hat{T}-\hat{T}_\infty)$ where $\gamma_T>0$ and $\gamma_T=-d\gamma/d\hat{T}$.

For the energy balance, $\hat{T}$ is nondimensionalized as $T=(\hat{T}-\hat{T}_\infty)/\triangle\hat{T}$, where $\triangle\hat{T}$ is the temperature increase at the heater. Equation (3) reduces to

$$T_{zz} = 0, \tag{15}$$

with the assumption that $\mathrm{PeCa}_0^{1/3} \ll 1$, where $\mathrm{Pe}=U\hat{h}_\infty/\alpha_{th}$ is the Peclet number. Energy transport by convection in the liquid is therefore neglected. Equation (7) becomes

$$T(x,y,z=0) = T_0(x), \tag{16}$$

and Eq. (17) reduces to

$$T_z^i + \mathrm{Bi}T^i = 0, \tag{17}$$

where $\mathrm{Bi}=\hat{h}_\infty H/k_{\mathrm{th}}$ is the Biot number.

Integrating Eq. (15) and applying Eqs. (16) and (17) yields an expression for the temperature of the liquid-gas interface,

$$T^i(x) = \frac{T_0(x)}{(1+\mathrm{Bi}h)}. \tag{18}$$

Recently reported three-dimensional numerical simulations of this flow configuration have shown that the capillary ridge is unstable to rivulet formation for Marangoni numbers greater than a critical value, and the ridge is unstable even for $\mathrm{Bi}=0$ [22]. The wave number of the preferred mode was found to be only slightly affected by variations of the Biot number for $\mathrm{Bi} \leqslant 0.1$. This present study is therefore restricted to the limit $\mathrm{Bi} \to 0$, for which Eq. (18) simplifies to $T^i(x)=T_0(x)$. Attention is focused on the transient dynamics of perturbations and the influence of substrate inclination angle on the rivulet instability, in addition to probing the similarities between the rivulet instability in flow over a heater and the fingering instability that develops at the advancing front of spreading films.

Integrating Eqs. (9)–(11) and using Eqs. (12)–(14), the velocity field is

$$\boldsymbol{u} = 3[\sin\theta \boldsymbol{e}_x + \nabla(\nabla^2 h - \mathrm{G}\cos\theta h)][h^2-(z-h)^2]/2 - 2\mathrm{M}\nabla T^i z. \tag{19}$$

Using the kinematic condition

$$\frac{\partial h}{\partial t} + \nabla \cdot \int_0^h \boldsymbol{u} dz = 0 \tag{20}$$

and Eq. (19), an equation governing the evolution of the interface shape is obtained,

$$\frac{\partial h}{\partial t} + \nabla \cdot [(\sin\theta \boldsymbol{e}_x + \nabla\nabla^2 h - \mathsf{G}\cos\theta \nabla h)h^3 - \mathsf{M}\nabla T^i h^2] = 0. \tag{21}$$

Substituting $h(x,y,t)=h_0(x,t)$ into Eq. (21) yields an equation that can be used to calculate the two-dimensional film profile for the base state,

$$\frac{\partial h_0}{\partial t} + \frac{\partial}{\partial x}[(\sin\theta + h_{0xxx} - \mathsf{G}\cos\theta h_{0x})h_0^3 - \mathsf{M}T_x^i h_0^2] = 0. \tag{22}$$

Although the base state is steady, $h_0(x,t)=h_0(x)$, the time dependence is retained in Eq. (22) to facilitate the numerical computation of the steady film profile. Because there are no temperature gradients far away from $x=0$, the film becomes flat, and

$$h_0(x \to \pm\infty) = 1. \tag{23}$$

These boundary conditions are implemented numerically as $h_0(x=\pm L)=1$ and $h_{0x}(x=\pm L)=0$, where $2L$ is the domain length, which is increased until there is no effect of L on the results.

Equation (22) was solved via the finite element method using FEMLAB 3.1 for different values of M with a prescribed temperature field $T_0(x)$ at the solid surface. A unit height profile was chosen as the initial condition for Eq. (22), and the equation was evolved in time until a steady profile was obtained. The accuracy of the method was assessed by examining the invariance of $\int_{-\infty}^{\infty}[MT_x^i/h_0+(1-h_0^3)\sin\theta/h_0^3]dx=0$. This property is guaranteed from Eq. (22) using Eq. (23), and the value of this integral was always less than 10^{-9}. Other tests of accuracy included convergence after mesh refinement and variation of the integration interval. Typically, about 1000 points were used for the computations, with local refinement of the mesh around the regions with steep gradients in the temperature or free-surface shape.

The linearized equation that governs a small perturbation to the film, $h_1(x,y,t)$, is obtained by expressing the film thickness $h(x,y,t)=h_0(x,t)+\epsilon h_1(x,t)\exp(iqy)$, where $\epsilon \ll 1$. Substituting into Eq. (21) and collecting $O(\epsilon)$ terms yields the linearized equation

$$\frac{\partial h_1}{\partial t} = \sum_{i=0}^{i=4} \mathbb{L}_i h_1^i, \tag{24}$$

where

$$\mathbb{L}_0 = -[-3h_{0x}\sin\theta/h_0^2 + \mathsf{M}(T_{0x}h_0)_x + q^2\mathsf{G}\cos\theta h_0^3 + q^4 h_0^3],$$

$$\mathbb{L}_1 = -[3\sin\theta/h_0 - 3h_0^2 h_{0x}(q^2 + \mathsf{G}\cos\theta) + \mathsf{M}T_{0x}h_0],$$

$$\mathbb{L}_2 = (2q^2 + \mathsf{G}\cos\theta)h_0^3,$$

$$\mathbb{L}_3 = -3h_0^2 h_{0x},$$

$$\mathbb{L}_4 = -h_0^3. \tag{25}$$

The boundary conditions for Eq. (24) are that h_1 is bounded as $x \to \pm\infty$. For the leading eigenvalue, the corresponding eigenfunction is flat far from $x=0$ ($h_{1x} \to 0$ as $x \to \pm\infty$). This system of equations when discretized in space using a fourth order, centered finite difference scheme can be written in vector form as

$$\frac{\partial \boldsymbol{h}_1}{\partial t} = \boldsymbol{A}\boldsymbol{h}_1, \tag{26}$$

where $\boldsymbol{A}$ is an autonomous matrix. Assuming exponential time dependence for h_1, $\boldsymbol{h}_1=\boldsymbol{\Phi}\exp(\beta t)$, yields the eigenvalue problem $\beta\boldsymbol{\Phi}=\boldsymbol{A}\boldsymbol{\Phi}$. The eigenvalues $\beta(q)$ of the matrix $\boldsymbol{A}$ were found using the MATLAB 6.5 function eig for different values of the wave number q.

III. UNPERTURBED FLOW

Base profiles are presented in Sec. III A, while the streamlines are discussed in Sec. III B. The plate is assumed vertical ($\theta=90°$) unless otherwise stated.

A. Base states

Two qualitatively different models for temperature profiles at the solid substrate are used in this work. A semi-infinite heater, which is similar to that used by Skotheim *et al.* [24] and Frank *et al.* [22], is modeled as

$$T_0(x) = 0.5[1 + \tanh(x)]. \tag{27}$$

Shown in Fig. 2(a) are base profiles for different M obtained by solving Eq. (22) with Eq. (27). The streamwise flow due to gravity is opposed by the thermocapillary stress $\tau = d\gamma/dT$ at the upstream edge of the heater, which decreases the streamwise velocity near the free surface. The film consequently thickens locally to maintain a constant flow rate ($Q=\int_{z=0}^{z=h} u dz$). When smoothed by capillary forces, this local thickening is manifested in a pronounced capillary ridge near the upstream edge of the heater. This ridge increases in amplitude as M increases and is susceptible to the formation of periodic rivulets aligned with the flow beyond a critical value of the Marangoni parameter, M_{crit}.

A finite-length heater is more relevant for many applications. The corresponding temperature profile is

$$T_0 = 0.5[\tanh(x+4) - \tanh(0.5x-4)]. \tag{28}$$

Base profiles for a film flowing over a finite heater are shown in Fig. 2(b). Because $dT_0/dx > 0$ at the upstream edge of the heater, $d\gamma/dx < 0$, and a capillary ridge appears as for the semi-infinite heater. At the downstream edge of the heater, $d\gamma/dx > 0$, and there is a depression in the free surface. The magnitude of the depression has a weaker dependence on M than that of the ridge and was found to have a minimal influence on the stability results.

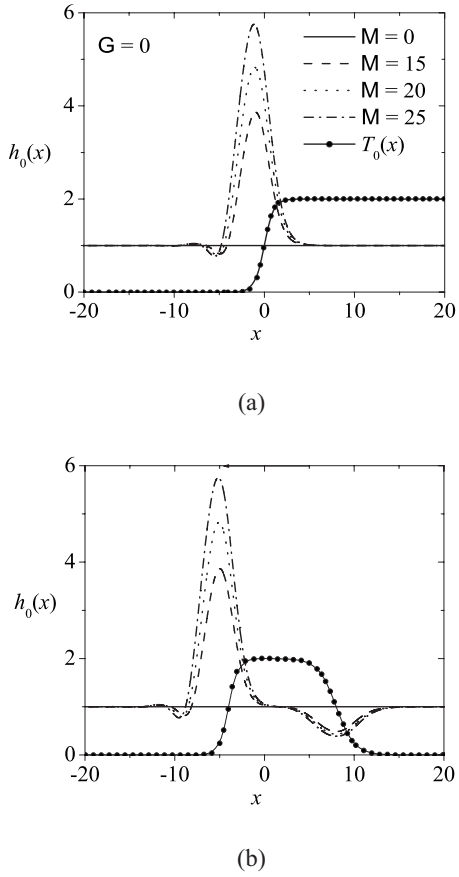

FIG. 2. Base profiles for different values of the Marangoni parameter M. (a) Semi-infinite heater. (b) Finite heater. The temperature profile at the solid substrate, $T_0(x)$, is superimposed to show the location of the capillary ridge relative to the heater.

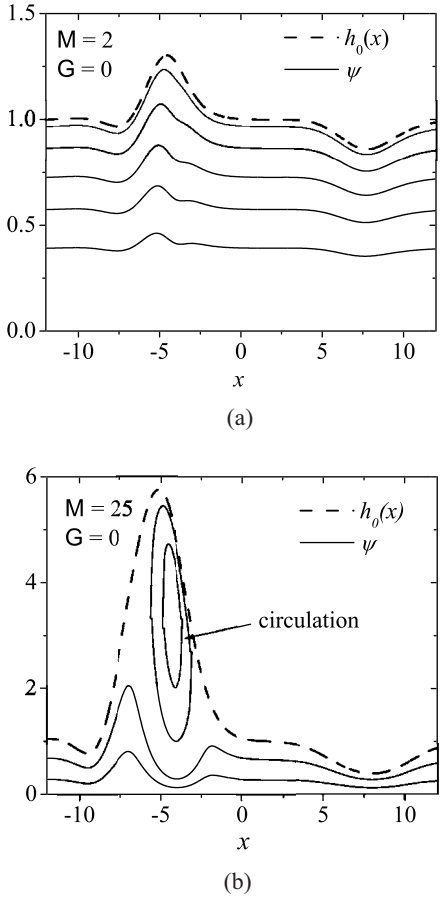

FIG. 3. (a) Base state and open streamlines for M=2 and G=0. (b) Base state and closed streamlines for M=25 and G=0, which illustrates the circulating flow beneath the capillary ridge.

B. Streamlines

For flow over topographical features of finite width, it was shown by Davis and Troian [27] that the flow is strongly stable to perturbations and that the streamlines showed no circulation under the ridge. The result was contrasted to the contact line motion of gravity driven films with an unstable capillary ridge, beneath which the streamlines are closed. When the capillary ridge was stabilized by hydrostatic pressure, the circulation disappeared and open streamlines were obtained.

For the present case of flow over a locally heated surface, streamlines can be determined from the velocity profile given by Eq. (19). The stream function $\psi(x,z)$, defined through $u=\partial\psi/\partial z$, is

$$\psi(x,z) = \frac{3}{2h_0^3}\left(h_0 z^2 - \frac{z^3}{3}\right) + \frac{\mathrm{M}T_{0x}}{2h_0}(h_0 z^2 - z^3), \qquad (29)$$

where there is implicit dependence on G through $h_0(x)$. Using this equation and solving for the streamlines, it was found that for $\mathrm{M}<2.97$ (with G=0), there are no closed streamlines and therefore no fluid circulation, as shown in Fig. 3(a). From the linear stability analysis, it was found that these base states are indeed strongly stable to perturbations, as reported in the next section. This observation is consistent with that discussed by Davis and Troian [27]. For larger Marangoni numbers, closed streamlines were found, which indicates fluid circulation under the ridge, but the ridge is still stable to perturbations. For the Marangoni number at which circulation begins, the velocity vector at the free surface changes sign at some value of x. Hence for circulation, $u[z=h_0(x)]\leqslant 0$ near the leading edge of the heater, which implies that $\mathrm{M}\geqslant 3\sin\theta/(T_{0x}h_0^2)$, which gives a criterion for M at the onset of fluid circulation and thus closed streamlines. For larger M at which the ridge is unstable, significant circulation appears beneath the ridge, as shown in Fig. 3(b), but the presence of closed streamlines is not directly linked to instability for continuous films flowing over differentially heated surfaces.

IV. STABILITY

The stability of the base states is explored using a modal linear stability analysis. A nonmodal, transient analysis is also used to determine the maximum amplification of perturbations and the most sensitive regions of the film.

A. Modal analysis

In the work of Kalliadasis *et al.* [25], both the discrete and continuous spectra of the linear operator $\mathbb{L}$ were computed,

though the corresponding eigenfunctions for the two spectra were not shown. The continuous spectrum corresponds to (stable) capillary waves that approach bounded oscillations as $x \to \pm\infty$. The shape, but not decay rate, of these modes is modified by the presence of the fluid ridge. The discrete spectrum corresponds to modes that localize at the capillary ridge and decay as $x \to \pm\infty$. These modes are responsible for the observed rivulet instability. While Kalliadasis *et al.* [25] used an integral momentum approach and retained convection in the energy equation, it is shown from the results presented here that the spectra (and the behavior of the eigenfunctions) are similar even for noninertial flows with energy convection neglected and a different temperature profile provided that the same boundary conditions are used for the perturbations.

For a flat film of unit thickness, the spectrum of eigenfunctions that approach bounded oscillations at the infinities consists of Fourier modes, $h_1 \sim \exp(\beta t + i\alpha x + iqy)$. In the present case, $T_{0x} \to 0$ and $h_0 \to 1$ as $x \to \pm\infty$. Away from the temperature gradient, the continuous modes will therefore have a similar structure to those for a flat film. The locus of the essential spectrum can be found by substituting $h_1(x,y,t) = \exp(\beta t + i\alpha x + iqy)$ into Eq. (24) as $x \to \pm\infty$, which yields

$$\beta = -(q^2+\alpha^2)^2 - (q^2+\alpha^2)\mathsf{G} - 3i\alpha. \tag{30}$$

The mode with the smallest decay rate corresponds to $\alpha = 0$, and the leading eigenvalue from the continuous spectrum is therefore given by $\beta = -q^4 - q^2\mathsf{G}$. The corresponding eigenfunction approaches constant values away from the heater, $h_1 \to c_\pm$ as $x \to \pm\infty$, and this mode is easily found with the boundary conditions $h_{1x}, h_{1xxx} \to 0$ as $x \to \pm\infty$.

The dispersion curves, $\beta(q)$, found from Eq. (26) are shown in Fig. 4 for different values of the Marangoni number M for the semi-infinite heater for the computational domain $x \in [-L, L]$. In the study of Skotheim *et al.* [24], periodic boundary conditions were used for the linear stability analysis, corresponding to an infinite array of temperature increases. The effect of domain length on the dispersion curves obtained by using periodic boundary conditions is plotted in Fig. 4(a) for $\mathsf{M}=25$. As the domain length increases, most of the dispersion curve slowly converges to the curve obtained by using the more appropriate boundary conditions that h_1 is bounded for $x \to \pm\infty$, but the analysis with periodic boundary conditions predicts instability for small q ($\beta(q) \geqslant 0$ for $0 \leqslant q \leqslant q'$). For h_1 bounded as $x \to \pm\infty$, instability is predicted for a finite band of q separated from zero, $\beta(q) > 0$ for $0 < q_{c1} < q < q_{c2}$, which is consistent with numerical simulations of the full Navier-Stokes and energy equations in three dimensions with applied perturbations of various q [22] and with the results of Kalliadasis *et al.* [25]. The effect of domain length on the dispersion curves for h_1 bounded as $x \to \pm\infty$ was negligible after $L=40$.

Shown in Fig. 4(b) is the dispersion curve corresponding to the largest eigenvalue for each q for $\mathsf{M}=25$ and $\mathsf{G}=0$ for a finite-width heater. The leading eivenvalue from the continuous spectrum that was computed numerically was found to agree with the predicted relation $\beta = -q^4$, which provides

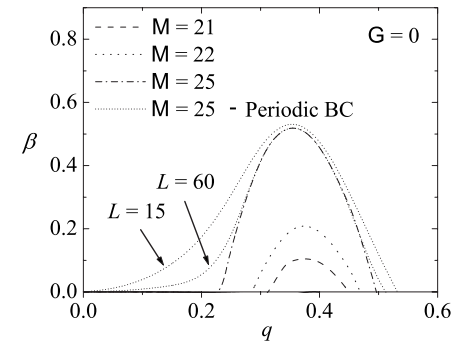

(a)

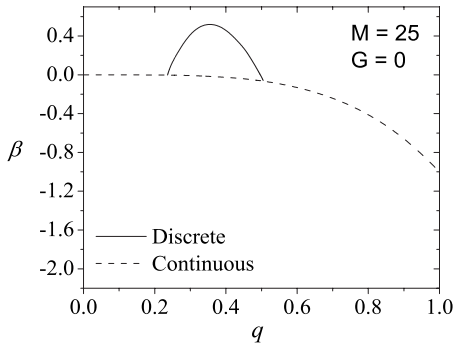

(b)

FIG. 4. (a) Dispersion curves for $\mathsf{G}=0$ with varying M. Results using periodic boundary conditions are included for comparison for a domain $x \in [-L, L]$. (b) Dispersion curves for $\mathsf{M}=25$ and $\mathsf{G}=0$ corresponding to the discrete and continuous modes. Additional (strongly stable) discrete modes are also found for $q > 1.7$ for a semi-infinite heater and $q > 1.5$ for a finite heater.

an additional check on the numerical methods. Like noninertial flows over topography [26,27], discrete modes are found above a large, threshold value of q ($\tilde{q}_{\text{crit}} = 1.7$ for a semi-infinite heater and $\tilde{q}_{\text{crit}} = 1.5$ for a finite heater), and these modes are highly stable to perturbations due to damping by surface tension. Unlike flow over topography, however, the capillary ridge induced by the heater is unstable for $\mathsf{M} > \mathsf{M}_{\text{crit}}$, with $\mathsf{M}_{\text{crit}} \approx 19.9$ for $\mathsf{G}=0$ for both semi-infinite and finite heaters. An additional band of (unstable) discrete modes appears for $q: 0 < q_{c1} < q < q_{c2}$, where q_{c1} and q_{c2} are the critical wave numbers that depend on M and G. From Fig. 4(a), it can be seen that beyond $\mathsf{M}=19.9$, a small increase in Marangoni number has a significant effect on the dispersion curve. For $\mathsf{M}=25$ and $\mathsf{G}=0$, $q_{c1}=0.236$, and $q_{c2}=0.504$, as seen in Fig. 4(b). The same qualitative behavior is observed for other choices of parameters that correspond to unstable films, but this band of discrete modes does not exist if the film is stable.

Shown in Fig. 5 are the shapes of selected leading eigenfunctions $\mathbf{\Phi}_0$ from the linear stability analysis. For $\mathsf{G}=0$ and $\mathsf{M}=25$, as shown in Fig. 5(a), $q=0.4$ corresponds to an unstable wave number. The eigenfunction exhibits a pronounced peak at the leading edge of the heater for $q=0.4$ and decreases to zero away from the heater. For the leading con-

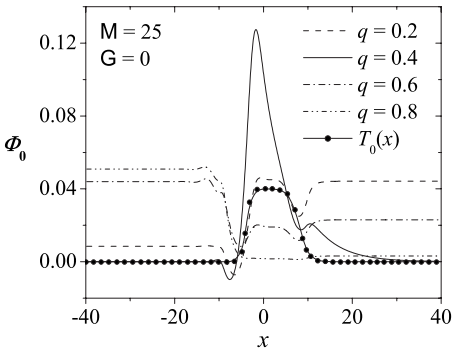

(a)

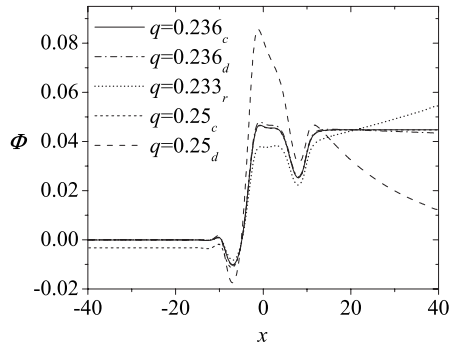

(b)

FIG. 5. (a) Leading eigenfunctions Φ_0 for $\mathsf{M}=25$ for a finite heater normalized such that $\int_{x=-40}^{x=40}|\Phi_0|^2dx=1$. (b) Structure of the leading discrete and continuous modes for $q\approx q_{c1}$ with $\mathsf{M}=25$ and $\mathsf{G}=0$. The subscripts c and d refer to continuous and discrete modes, respectively, while r denotes the structure that replaces the discrete mode for $q<q_{c1}$ upon crossing the continuous spectrum.

tinuous eigenfunctions corresponding to stable wave numbers, no significant peak is observed, and the eigenfunctions attain constant values away from the heater. This behavior is analogous to flow over topographical features [26,27], which is also formulated in an infinite domain. In the present case the Marangoni stress is responsible for the capillary ridge, whereas for flow over topography the capillary pressure from the edges of the feature leads to the formation of a capillary ridge. Similar to flow over topography [27], open streamlines were observed for the stable flows. The presence of closed streamlines did not guarantee instability, however.

The structure of the discrete and continuous modes near $q=q_{c1}$ is shown in Fig. 5(b). For $q=q_{c1}=0.236$, the discrete and leading continuous mode have the same shape for most of the domain, and $c_-=0$. The discrete mode decays very slowly to zero as $x\to\infty$, while the continuous mode attains the constant value $c_+>0$. For $q=0.233<q_{c1}$, $c_->0$, but the continuous mode is indistinguishable from the result for $q=0.236$ near the heater and as $x\to\infty$ (not shown in plot). A discrete mode was not found for $q=0.233$, as the corresponding structure exponentially blows up as $x\to\infty$, as shown by the $q=0.233_r$ curve in Fig. 5(b), which was determined using exponentially weighted eigenfunctions to filter away this unbounded growth [25]. For $q=0.25>q_{c1}$, $c_-<0$, but the continuous mode has nearly the same shape as for $q=0.236$ near the heater and as $x\to\infty$. The decay of the discrete mode for $q=0.25$ as $x\to\infty$ is apparent. Similar behavior occurs for $q\approx q_{c2}$, as c_- changes sign between q_{c1} and q_{c2}. The discrete mode decays much more rapidly when q is away from q_{c1} or q_{c2}, which is consistent with the observation of Kalliadasis and Homsy [26] for flow over topography (at large q for which the discrete modes exist). As for flow over topography, discrete modes also exist beyond a critical wave number $\tilde{q}_c>1$, but those modes are highly stable to perturbations. For the semi-infinite heater the critical wave number is $\tilde{q}_c=1.7$, and for the finite heater $\tilde{q}_c=1.5$. The continuous modes are always stable because the instability does not affect the film far from the heater, whereas some of the discrete modes lead to instability, as was also observed by Kalliadasis *et al.* [25]. Because the results for finite and semi-infinite heaters are similar, results are presented only for finite heaters in what follows.

1. Effect of temperature profile

Shown in Fig. 6 is the effect of the steepness of the temperature increase at the heater on the film profile and dispersion curves. The temperature of the solid surface was modeled as

$$T_0(x)=0.5[\tanh(ax+d)-\tanh(0.5x-4)]. \tag{31}$$

Varying d corresponds to varying the "width," or streamwise extent, of the heater. For $d\in[3,10]$, the distance between the capillary ridge and depression increases with d, as expected, but d has no effect on the shape or amplitude of the capillary ridge or the dispersion curves. As a is increased, the capillary ridge becomes steeper and higher and shifts downstream, as shown in Fig. 6(a). The height of the ridge saturates for $a>5$. The dispersion curves are also strongly affected by the value of a, as shown in Fig. 6(b). For $\mathsf{M}=25$ and $\mathsf{D}=0$, the film is stable for the gradual temperature gradient corresponding to $a=0.5$ but is unstable for larger a. The influence of a on $\mathsf{M}_{\mathrm{crit}}$ is shown in Fig. 6(c). The critical Marangoni number decreases with a but remains constant for $a\geqslant 5$, which is the same value above which the capillary ridge is unaffected by a.

2. Effect of substrate inclination angle

Shown in Fig. 7 is the effect of the substrate inclination angle θ on the largest eigenvalue from the linear stability analysis for $\mathsf{M}=25$. As θ decreases, the hydrostatic component of the pressure in the film ($\mathsf{G}\cos\theta$) increases, which would tend to flatten the capillary ridge induced by the Marangoni stress at the heater. Because the component of gravity parallel to the substrate, which drives the flow, is proportional to $\sin\theta$ [$U=\rho g\hat{h}_\infty^2\sin\theta/(3\mu)$], however, the driving force decreases relative to the Marangoni stress. These two considerations have a competing influence on the film shape, and the capillary ridge increases in width and amplitude as θ decreases for small G. The ridge becomes flatter for larger G and small θ, for which the hydrostatic component of pressure is more significant. This trend agrees with experimental results [30].

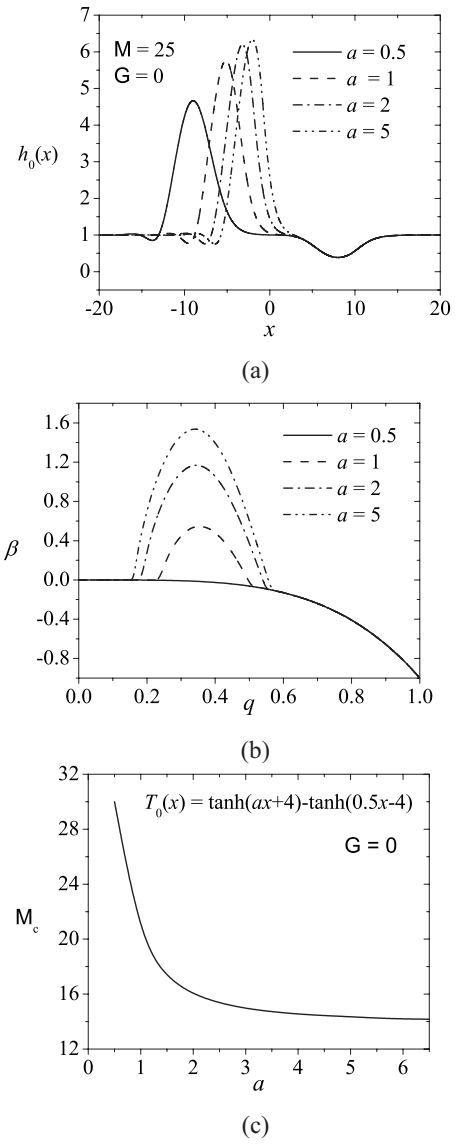

FIG. 6. Effect of the steepness parameter a on the (a) film profile and (b) dispersion curves for M=25 and G=0. (c) Critical Marangoni number M_{crit} vs a.

For $G \leqslant 0.1$ the variation of $\beta_{max} \equiv \max_q(\beta)$ with θ is nonmonotonic. As θ decreases from 90° and the ridge becomes larger, β increases. Beyond some threshold value of θ, β then decreases for each G, as shown in Fig. 7(a). For $G > 0.1$, β_{max} decreases monotonically with θ. The film is stable for $\theta \leqslant 15°$ for G=0.3, and $\beta_{max} \to 0$ as $\theta \to 0$ for all G, as a horizontal film is stable with respect to rivulet formation because there is no flow, although the ridge may be susceptible to a Rayleigh instability. Also, as θ decreases, the wave number (q_{max}) of the most unstable mode decreases, which corresponds to a larger wavelength of the observed instability. A plot of q_{max} vs θ is shown in Fig. 7(b). For small G these results are in reasonable agreement with the experimental result $q_{max} \propto (\sin\theta)^{1/2}$ [31]. These stability results are consistent with those for a liquid film spreading along an inclined plane [23,28,32] because the governing forces are the same. Although the origin of the capillary

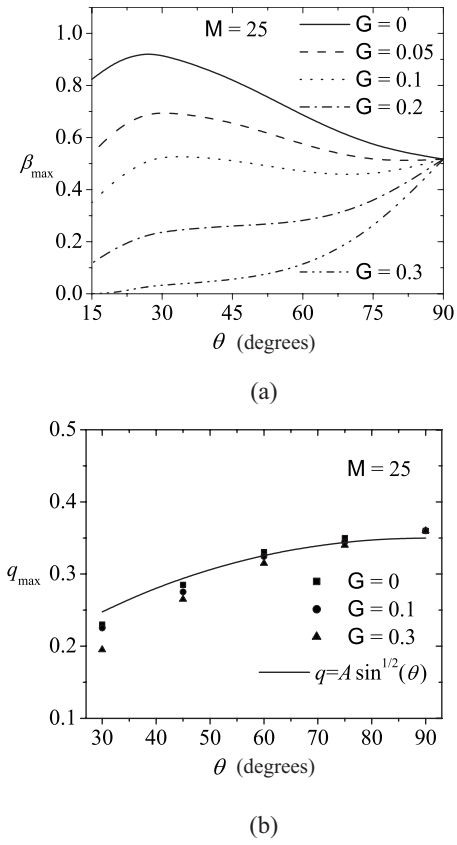

FIG. 7. (a) Effect of substrate inclination angle θ (in degrees) on the largest eigenvalue, β_{max}, for various G. (b) Wave number q_{max} corresponding to β_{max} vs θ. For small G the trend is well described by the experimentally observed relation $q \propto \sin^{1/2}\theta$.

ridge is different, the appropriate length scale l_c is determined from a balance of viscous and capillary forces, and gravity drives the flow.

B. Transient amplification: Nonmodal analysis

Thin liquid films with thermocapillary stresses give rise to non-normal linear operators $\boldsymbol{A}$ when the base states are spatially nonuniform [33–37]. In extreme cases, the transient amplification of perturbations to the film might lead to instability in a flow predicted to be linearly stable or overwhelm the modal growth at early times in a linearly unstable flow, possibly resulting in a different instability wavelength than predicted by modal analysis [38,39]. Even if the transient growth is less significant, the nonmodal analysis provides insight into the regions of the film that are most sensitive to perturbations (which are evident from the structure of the eigenfunctions only for normal systems).

The solution to Eq. (26) is

$$\boldsymbol{h}_1(t) = \exp(\boldsymbol{A}t)\boldsymbol{h}_1(t=0), \tag{32}$$

where $\boldsymbol{h}_1(t=0)$ is the initial perturbation applied to the base state. The maximum amplification σ_{max} of an initial perturbation over the time interval t is then given by

$$\sigma_{\max}(t) = \sup_{\boldsymbol{h}_1(t=0)\neq\mathbf{0}} \frac{\|\boldsymbol{h}_1(t)\|}{\|\boldsymbol{h}_1(t=0)\|} = \|\exp(t\boldsymbol{A})\|, \quad \epsilon[0,t), \tag{33}$$

where $\|\cdot\|$ represents the l_2 norm. The matrix $\boldsymbol{A}$ has the similarity transform $\boldsymbol{A}=\boldsymbol{S}\boldsymbol{\Delta}\boldsymbol{S}^{-1}$, where $\boldsymbol{S}$ is the matrix whose columns are the normalized eigenvectors $\boldsymbol{\Phi}_i$ of $\boldsymbol{A}$ in order of growth rate and $\boldsymbol{\Delta}$ is the diagonal matrix of the associated eigenvalues [40]. It follows that

$$\exp(\beta t) \leqslant \|\exp(t\boldsymbol{A})\| = \|\boldsymbol{S}\exp(t\boldsymbol{\Delta})\boldsymbol{S}^{-1}\| \leqslant \|\boldsymbol{S}\|\|\boldsymbol{S}^{-1}\|\exp(\beta t), \tag{34}$$

where β is the leading entry of $\boldsymbol{\Delta}$, $\{\Delta\}_{11}$. If $\boldsymbol{A}$ is normal, $\boldsymbol{S}$ is unitary, and $\|\exp(t\boldsymbol{A})\| = \exp(\beta t)\,\forall\, t$. If $\boldsymbol{A}$ is non-normal, however, the eigenvectors are not orthogonal, and the norm of $\boldsymbol{S}$ and $\boldsymbol{S}^{-1}$ can be very large. Perturbations could therefore be amplified by several orders of magnitude and induce nonlinear effects [39]. As $t\to\infty$ the first column of $\boldsymbol{S}$ and the first row of $\boldsymbol{S}^{-1}$ exponentially dominate, and it follows from Eqs. (33) and (34) that

$$\lim_{t\to\infty} \sigma_{\max} = \|\boldsymbol{\Phi}_0\|\|\hat{\boldsymbol{\Phi}}_0\|\exp(\beta t), \tag{35}$$

where $\hat{\boldsymbol{\Phi}}_0$ is the leading eigenvector of the adjoint of $\boldsymbol{A}$ normalized such that $\langle\boldsymbol{\Phi}_0,\hat{\boldsymbol{\Phi}}_0\rangle=1$.

The maximum amplification of perturbations to the film is plotted in Fig. 8(a) for $\mathsf{M}=25$ and in Fig. 8(b) for $\mathsf{M}=15$. Each point on these curves represents the maximum amplification of a different initial condition, which is optimal for the time interval $[0,t)$. The slope of each curve as $t\to\infty$ recovers the leading eigenvalue of $\boldsymbol{A}$, which provides an additional check on the accuracy of the computations. These curves indicate that modal growth or decay (characterized by the leading eigenvalue β) occurs after a brief transient period, and the nonmodal, transient amplification is less than an order of magnitude, which suggests that nonlinear effects are not important in the initial development of the instability. The transient growth for $\mathsf{M}=15$, which is asymptotically stable, is insufficient to induce nonlinear effects and instability by a nonmodal mechanism. Indeed, several nonlinear simulations of $h(x,y,t)$ vs t were performed for $\mathsf{M}<\mathsf{M}_{\text{crit}}$ with imposed sinusoidal perturbations of various q, and rivulets could not be initiated in these linearly stable films even with a perturbation amplitude of one-half the unperturbed film thickness. The transient amplification is larger than for flow over topography [27] but considerably less than for spreading films [32,34–36,41]. The secondary amplification beginning at $t\approx 12$ for $q=0.20$ in Fig. 8(a) is not seen in transient dynamics of driven liquid films [34–36,41] or flow over topographical features [27] and is explained below in the context of the optimal perturbations to the film.

Shown in Fig. 9 is the maximum transient amplification with the modal growth factored out, $\delta=\|\exp(t\boldsymbol{A})\|\exp(-\beta t)$, vs L, where $2L$ is the domain length, for various q. The variation of this purely nonmodal amplification with the domain length is accurately characterized by $\delta\propto L^{1/2}$ for $q=0$ and $q=0.6$ but is independent of domain length for $q=0.3$ for

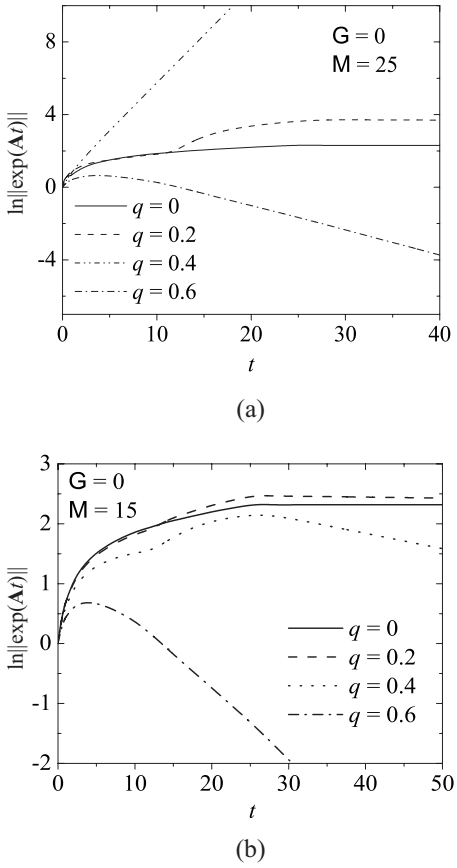

FIG. 8. Maximum transient amplification of spanwise perturbations for $\mathsf{G}=0$ and (a) $\mathsf{M}=25$ and (b) $\mathsf{M}=15$.

$L>30$. For $q=0$ and $q=0.6$, discrete modes are absent and only stable, continuous modes exist, as shown in Fig. 4(b). For the continuous spectrum, the disturbances are global and do not localize around the capillary ridge. Restricting the size of the domain in computations of the transient amplification therefore restricts the global extent of disturbances.

The dependence of δ on L can thus be explained by the arguments of Grigoriev [41] in the context of spreading liq-

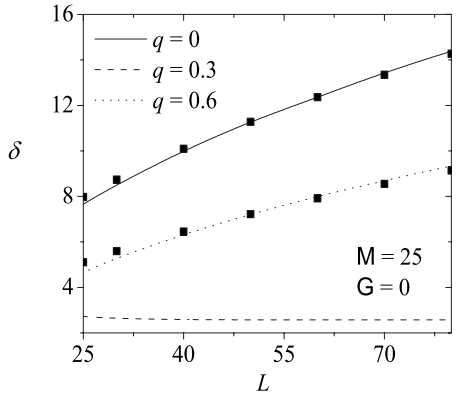

FIG. 9. (a) Maximal nonmodal amplification, $\delta \equiv \|\exp(t\boldsymbol{A})\|\exp(-\beta t)$, for $q=0$, 0.3, and 0.6 as a function of the domain size L for $\mathsf{G}=0$ and $\mathsf{M}=25$. The symbols correspond to $\delta \propto L^{1/2}$.

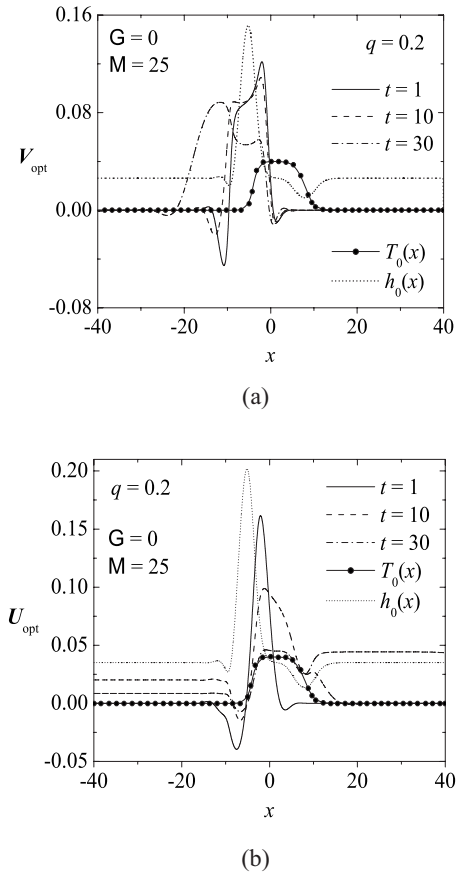

FIG. 10. (a) Optimal initial disturbance $\boldsymbol{V}_{\text{opt}}$ and (b) corresponding evolved state $\boldsymbol{U}_{\text{opt}}$, after time t for a perturbation of wave number $q=0.2$ applied to the base state with $\mathsf{G}=0$ and $\mathsf{M}=25$.

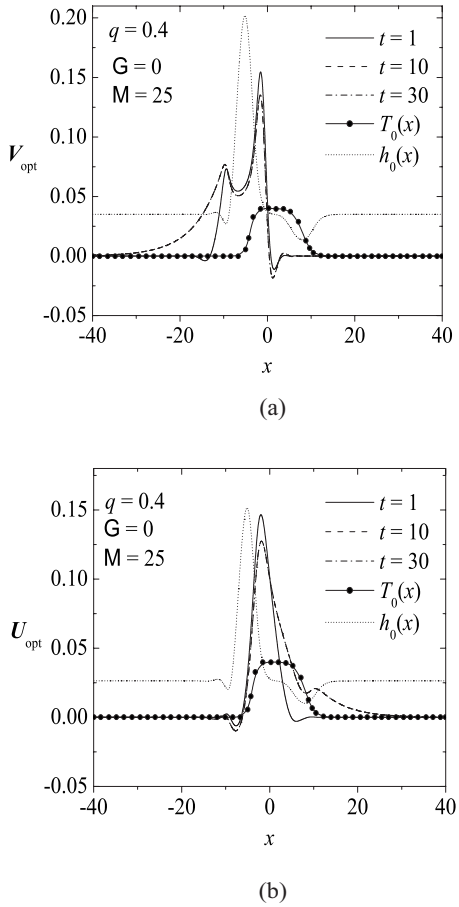

FIG. 11. (a) Optimal initial disturbance $\boldsymbol{V}_{\text{opt}}$ and (b) corresponding evolved state $\boldsymbol{U}_{\text{opt}}$, after time t for a perturbation of wave number $q=0.4$ applied to the base state with $\mathsf{G}=0$ and $\mathsf{M}=25$.

uid films. From Eq. (35) $\delta=\|\boldsymbol{\Phi}_0\|\|\hat{\boldsymbol{\Phi}}_0\|$. When discrete modes are absent, $\boldsymbol{\Phi}_0$ attains the constant values $c_\pm$ away from the heater, so $\|\boldsymbol{\Phi}_0\|=(\int|\boldsymbol{\Phi}_0|^2dx)^{1/2}\propto L^{1/2}$. The corresponding adjoint eigenvector $\hat{\boldsymbol{\Phi}}_0$ essentially has finite support, so $\|\hat{\boldsymbol{\Phi}}_0\|$ =const for sufficiently large L, which results in $\delta\propto L^{1/2}$, as observed in Fig. 9. (These arguments are reversed and restricted to $q\to 0$ for spreading films [41].) For discrete modes, however, the disturbances localize around the heater and have finite support. Once the domain is sufficiently long to allow these modes to decay as $x\to\pm\infty$ (which makes the eigenvalues and eigenfunctions independent of L), δ is also independent of L. This pronounced difference in the dependence of δ on L for stable vs unstable modes is not observed for spreading films [36,41] because the leading eigenfunction for each q is discrete.

C. Optimal perturbations

To determine the evolution of an optimal initial perturbation into its final state after time t, the singular value decomposition of $\exp(t\boldsymbol{A})$ is calculated according to [39]

$$\exp(t\boldsymbol{A})=\boldsymbol{U}\boldsymbol{\Sigma}\boldsymbol{V}^\dagger. \tag{36}$$

The columns of the unitary matrix $\boldsymbol{V}$ are the complete set of (orthogonal) initial states, and the columns of the unitary matrix $\boldsymbol{U}$ are orthonormal basis vectors that span the range space of final states. The diagonal matrix $\boldsymbol{\Sigma}$ contains elements σ_i that characterize the amplification of each corresponding initial state during the specified time interval. The vectors $\boldsymbol{V}_i$ form the columns of $\boldsymbol{V}$, and the optimal perturbation at a specified time, $\boldsymbol{V}_{\text{opt}}\equiv\boldsymbol{V}_1$, is the initial condition that undergoes the maximum growth over the time interval t. This maximum growth is denoted by the leading singular value, $\sigma_{\max}(t)\equiv\|\exp(t\boldsymbol{A})\|$ and corresponds to one point in Fig. 8. As $t\to\infty$, $\boldsymbol{U}_{\text{opt}}$ asymptotes to the eigenfunction that describes rivulet formation in the spanwise direction.

Shown in Figs. 10 and 11 are the optimal initial perturbations and the evolved states for $q=0.2$ and $q=0.4$. The optimal perturbations are located at the leading edge of the heater and extend upstream such that they are convected by the flow to the leading edge of the heater, or forward portion of the capillary ridge, at which the thermocapillary stress opposes the bulk flow. For $q=0.2$, which is asymptotically stable, $\boldsymbol{V}_{\text{opt}}$ is located at the leading edge of the heater for small t and extends a distance $w\approx 10l_c$ upstream, as shown in Fig. 10. Perturbations to this region of the film therefore undergo the largest growth over short time intervals $t\leqslant 10$. For larger t, $\boldsymbol{V}_{\text{opt}}$ extends and migrates further upstream such that it undergoes transient amplification when it is convected to the heater later in the dynamics. This migration reflects the

TABLE I. Terms contributing to the energy production rate of perturbations to the film and their physical interpretation.

Term	Expression	Physical meaning
1	$-(h_0^3 h_{1xxx})_x$	Capillary flow in x direction induced by perturbation curvature variation in x
2	$q^2(h_0^3 h_{1x})_x$	Capillary flow in x direction due to streamwise change in transverse perturbation curvature
3	$-3(h_0^2 h_1 \sin\theta)_x$	Flow in x direction due to gravity
4	$-(3h_0^2 h_{0xx} h_1)_x$	Capillary flow in x direction driven by the base-state capillary pressure gradient acting on the perturbation
5	$q^2 h_0^3 h_{1xx}$	Capillary flow in y direction induced by perturbation curvature in x
6	$-q^4 h_0^3 h_1$	Capillary flow in y direction induced by perturbation curvature in y
7	$2\mathsf{M}(T_{0x} h_0 h_1)_x$	Thermocapillary flow in x direction due to streamwise temperature variations
8	$\mathsf{G}(h_0^3 h_{1x} \cos\theta)_x$	Flow in x direction due to hydrostatic pressure of perturbation
9	$3\mathsf{G}(h_0^2 h_{0x} h_1 \cos\theta)_x$	Flow in x direction due to hydrostatic pressure of base-state acting on perturbation
10	$-q^2 \mathsf{G} \cos\theta h_0^3 h_1$	Flow in y direction due to hydrostatic pressure and perturbation thickness variation

global nature of disturbances for stable q (characterized by the continuous spectrum). The evolved states $\boldsymbol{U}_{\text{opt}}(t)$ initially localize at the heater but broaden to encompass the entire film as $t\to\infty$. By $t=30$, $\boldsymbol{U}_{\text{opt}}$ is indistinguishable from the eigenfunction $\boldsymbol{\Phi}_0$. The growth rate is largest as the perturbation encounters the forward portion of the capillary ridge above the heater, and the disappearance of the maximum in $\boldsymbol{U}_{\text{opt}}$ at the leading edge of the heater indicates that a perturbation to that region of the flow would have decayed by $t=30$.

The structure of $\boldsymbol{V}_{\text{opt}}$ and $\boldsymbol{U}_{\text{opt}}$ for the unstable wave number $q=0.4$, which are plotted in Fig. 11, is significantly different. The optimal perturbation for $t=1$ has a sharp peak at the leading edge of the heater and extends upstream about $w=15l_c$ units. As t increases, $\boldsymbol{V}_{\text{opt}}$ broadens somewhat upstream but retains the strong peak at the leading edge of the heater. For $t\geqslant 5$, $\boldsymbol{V}_{\text{opt}}$ is constant, and its structure reveals that perturbations applied to the portion of the film from $-20\leqslant x\leqslant 0$ are amplified most strongly, with the forward portion of the capillary ridge the most sensitive region to perturbations. These results suggest that the rivulet instability might be suppressed by appropriate modulation of the flow in this region of the film. For example, Frank [42] recently found using three-dimensional simulations that the value of M_{crit} could by doubled by using a feedback control for the temperature profile, and other mechanisms of modulating the flow are also possible. The evolved state $\boldsymbol{U}_{\text{opt}}$ is focused at the forward portion of the capillary ridge, or leading edge of the heater. For $t\geqslant 5$, $\boldsymbol{U}_{\text{opt}}$ is constant and indistinguishable from the leading eigenfunction. This rapid asymptote to the modal behavior corresponds to the small non-modal growth found for unstable q in Fig. 9 and occurs because of the near orthogonality between the (discrete) leading eigenfunction and the stable, continuous modes.

In Fig. 8(a), the transient curve for $q=0.2$ exhibits interesting behavior at $t\approx 10.8$. The evolved optimal perturbation at $t=t^*=10.8$, given by $\boldsymbol{U}_{\text{opt}}(t^*)=\exp(t^*\boldsymbol{A})\boldsymbol{V}_{\text{opt}}(t^*)$ was computed to confirm that this jump in the amplification ratio occurs at the time when $\boldsymbol{U}_{\text{opt}}$ interacts with the capillary ridge. The amplification of $\boldsymbol{V}_1$ and $\boldsymbol{V}_2$ is similar for $0\leqslant t<10.8$. By $t=10.8$, $\boldsymbol{U}_2$ has been convected past the capillary ridge, while $\boldsymbol{U}_1$ encounters the ridge and is amplified more strongly, after which $\sigma_1\gg\sigma_2$. This competing amplification of $\boldsymbol{V}_1\equiv\boldsymbol{V}_{\text{opt}}$ is responsible for the jump in the curve for $q=0.2$ at $t=10.8$ in Fig. 8(a) and is observed for q near q_{c1} and q_{c2}, where the dispersion curve bifurcates into continuous and discrete eigenmodes.

D. Energy analysis

Following Spaid and Homsy [28], the exponential growth rate β of perturbations can be interpreted as an energy production rate $\dot{E}$. The contributions of the individual terms in the disturbance operator $\mathbb{L}$ to $\dot{E}$ can be isolated to infer the influence of various physical mechanisms on the instability. The terms in Eq. (24) make contributions $\dot{E}_n$ to $\dot{E}$, which can be found from [28]

$$\dot{E}_n = \frac{\langle \boldsymbol{\Phi}_0, \mathcal{L}_n \boldsymbol{\Phi}_0 \rangle}{\langle \boldsymbol{\Phi}_0, \boldsymbol{\Phi}_0 \rangle}, \tag{37}$$

where $\langle .,. \rangle$ represents the inner product. Each $\mathcal{L}_n$ is a group of terms in $\mathbb{L}$ listed in Table I along with its physical meaning. These terms depend nonlinearly on the base flow solution, $h_0(x)$, and perturbation wave number q. Terms that make a negative energy contribution are stabilizing, while terms corresponding to a positive $\dot{E}_n$ are destabilizing. Noting that $\mathbb{L}=\Sigma\mathcal{L}_n$, it follows directly from Eq. (37) that $\Sigma\dot{E}_n=\beta$.

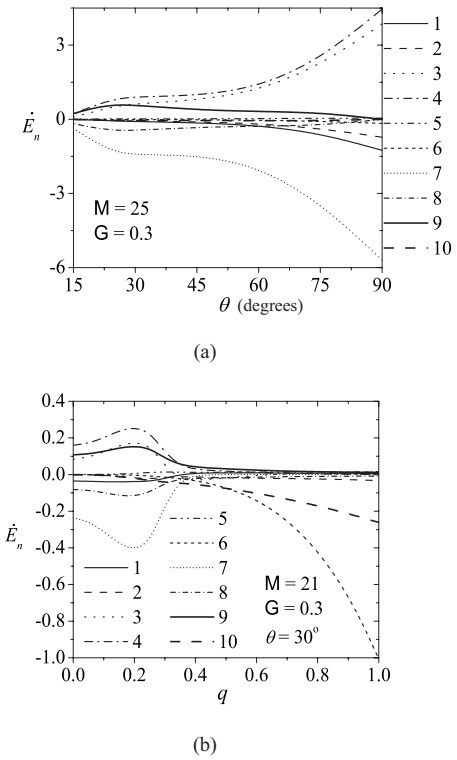

FIG. 12. Energy analysis results. (a) $\dot{E}_n$ for $q=q_{\max}$ vs θ (in degrees) for $\mathsf{G}=0.3$ and $\mathsf{M}=25$. (b) $\dot{E}_n$ vs q for $\mathsf{G}=0.3$, $\mathsf{M}=21$, and $\theta=30°$.

Shown in Fig. 12(a) is $\dot{E}_n$ for $q=q_{\max}$ vs θ with $\mathsf{M}=25$ and $G=0.3$. For a vertical substrate with $\theta=90°$, the two strongly destabilizing terms are term 3, the streamwise flow from gravity induced by the variation in the film thickness from the perturbation, and term 4, the streamwise flow from the capillary pressure gradient of the base state acting on the perturbation. The largest stabilizing influence is from term 7, the streamwise Marangoni flow from the change in film thickness induced by the perturbation. Term 1, the streamwise capillary flow induced by the streamwise perturbation curvature and term 2, the streamwise capillary flow induced by the streamwise change in the transverse curvature of the perturbation, are also stabilizing. All terms corresponding to flow in the transverse y direction induced by a perturbation do not make significant contributions to $\dot{E}$ for $\mathsf{Bi}=0$, although they can provide the dominant contributions to the instability for $\mathsf{Bi}\neq 0$ [24].

As θ decreases, the magnitude of terms 1–4 and 7 decreases. The streamwise component of gravity decreases with $\sin\theta$, so term 3 is less destabilizing. The shape of the ridge changes as hydrostatic pressure modifies the base state, and terms 1, 2, 4, and 7 decrease in magnitude. Term 9, the streamwise flow due to the influence of the base-state hydrostatic pressure on the perturbation, becomes more destabilizing. Term 8, the streamwise flow from the hydrostatic pressure of the perturbation becomes more stabilizing, and the film is stable for $\theta\leqslant 15°$ even though a ridge still exists.

Shown in Fig. 12(b) is $\dot{E}_n$ vs q for a film stabilized by hydrostatic pressure. For $q\leqslant 0.35$, terms 3, 4, and 9 are destabilizing, but terms 1, 7, and 8 compensate and result in a stable film. For larger q, the transverse capillary flow from terms 6 and 10 dominates and is strongly stabilizing. These terms correspond to the decay of capillary waves on a flat film with additional stabilization from hydrostatic pressure.

V. DISCUSSION

This analysis predicts that the wavelength of the instability is $\lambda_{\max}=(2\pi/q_{\max})l_c\propto\gamma_0^{1/3}$, which is in good agreement with the result $\lambda_{\max}\propto\gamma_0^{0.365}$ reported by Frank and Kabov [22]. If the plate is inclined at angle θ from the horizontal, the instability wavelength has been observed in experiments to grow considerably as θ is decreased, $\lambda_{\max}\propto(\sin\theta)^{-1/2}$. As shown in Fig. 7(b), this relation is consistent with the theoretical predictions for $30°\leqslant\theta\leqslant 90°$ and small G. In addition, the flow is predicted to be unstable above a critical Marangoni number for a finite band of wave numbers separated from zero, which agrees with the results of Frank and Kabov [22]. The marginal stability curves predicted by the lubrication model also agree qualitatively with those reported by Frank and Kabov [22], although differences in the temperature profile at the solid surface and the values of the dimensionless parameters preclude a quantitative comparison.

This lubrication model is similar to that used by Skotheim *et al.* [24], but utilizes different scalings (l_c vs length scale of the temperature gradient) and retains the hydrostatic pressure terms. More significantly, the present analysis requires that disturbances to the film be bounded (but oscillatory) as $x\rightarrow\pm\infty$ to be consistent with the Fourier modes that comprise the continuous spectrum for the flat regions of the film away from the heater, while Skotheim *et al.* [24] employed periodic boundary conditions for both the base state and linear stability analysis. The predictions of the model presented here agree qualitatively with those of Kalliadasis *et al.* [25], who used a qualitatively different temperature profile, developed an integral momentum approach, retained convection in the energy equation, and used a large value of the Biot number ($\mathsf{Bi}=1$) in their analysis. This agreement results from the use of the same boundary conditions that h_1 is bounded as $x\rightarrow\pm\infty$ for the linear stability analysis. In particular, a continuous and discrete spectrum were found, although the two critical wave numbers q_{c1} and q_{c2} are specific to the present analysis. Kalliadasis *et al.* [25] also found (stable) discrete modes for $\mathsf{M}<\mathsf{M}_{\mathrm{crit}}$.

The prediction for $\lambda_{\max}$ is similar to that found for the capillary ridge that forms in a gravity-driven fluid sheet spreading down an inclined plane [23], $\lambda_{\max}\propto\hat{h}_\infty(3\mathsf{Ca})^{-1/3}\propto\gamma_0^{1/3}$. These predictions are similar because the streamwise length scale, l_c, that is relevant to the capillary ridge is found from a balance of viscous and capillary forces. The origin of the ridge is different, as it is not induced by a thermocapillary flow from nonuniform heating but as a response of the free surface to the pressure field near the contact line in the spreading film. Once the ridge has formed, however, the mobility differences from perturbed regions near the front of the ridge are destabilizing for both problems. For flow over the heater, the streamwise capillary flow induced by the base-

state capillary-pressure gradient acting on the perturbation is also strongly destabilizing.

This flow over a locally heated surface is similar to noninertial flows over topography [26,27], in which the topographical feature induces a capillary ridge. The capillary pressure gradient from the (fixed) substrate topography produces a restoring flow that suppresses transverse perturbations to the ridge, and those flows were found to be strongly stable to perturbations. The thermocapillary stress from the heater has a similar stabilizing influence on perturbations. This thermocapillary stress, however, also leads to the formation of the ridge, and once the ridge becomes sufficiently large it is destabilized by mobility differences in the perturbed film and the interaction of perturbations with the streamwise capillary pressure gradient due to the curvature of the (deformable) capillary ridge.

VI. CONCLUSION

The stability of a liquid film flowing over a locally heated surface was considered using a lubrication analysis. The thermocapillary stress at the heater leads to the formation of a pronounced capillary ridge, which was found to be unstable to spanwise perturbations above a critical Marangoni number for a finite band of wave numbers separated from zero. These results agree with published experiments and direct numerical simulations [22]. This rivulet instability, which occurs even for vanishing Biot number, is due to mobility differences in the perturbed ridge and the effect of the capillary pressure gradient on perturbations and is distinct from the classical thermocapillary instability at finite Biot number. Because the instability is linked to the flow in the capillary ridge, its wavelength was found to scale with the dynamic capillary length, as for the fingering instability of an isothermal capillary ridge in a film spreading down an inclinded plane [23]. The wavelength of the instability increases as the plate becomes more horizontal, in agreement with experimental results [31]. The decrease in inclination angle has a nonmonotonic effect on the growth rate of perturbations for small values of the hydrostatic parameter G but has a monotonic stabilizing influence for larger G, which was explored through an energy analysis.

The linear stability problem was formulated to allow for disturbances that are bounded (but do not necessarily decay) at the infinities. The operator that governs the linearized system has both a discrete and an essential spectrum, which is consistent with results from an integral momentum analysis by Kalliadasis *et al.* [25]. The essential spectrum consists of eigenfunctions that approach bounded oscillations at the infinities. Although their shape is modified by the capillary ridge near the heater, their corresponding spectrum is described by the dispersion relation of a flat film, and these modes are always stable. The discrete spectrum exists above a critical Marangoni number for a finite band of wave numbers separated from zero, and these modes are linked to the rivulet instability. Highly stable discrete modes are also found above a (large) threshold value of the wave number, which is consistent with the stable, noninertial flows over topographical features [26,27]. Differences in the boundary conditions for the stability analysis were found primarily responsible for qualitative differences between published results based on lubrication [24] and integral boundary-layer [25] models.

Because the linearized disturbance operator is nonnormal, a transient, nonmodal analysis was used to study the short-time dynamics of perturbations. The transient amplification of perturbations was found to be essentially negligible for unstable wave numbers because the (unstable) discrete eigenfunction is nearly orthogonal to the (stable) continuous modes. Weak transient amplification was found for stable wave numbers, and its dependence on the domain length was captured by analyzing the shape of the leading eigenfunctions of the disturbance operator and its adjoint. The structure of optimal perturbations was computed to elucidate the regions of the film that are most sensitive to perturbations, which suggests ways to stabilize the film by appropriately modulating the flow in these regions.

ACKNOWLEDGMENTS

J.M.D. kindly acknowledges support from a 3M Nontenured Faculty Grant, from the National Science Foundation CBET division, and from the Camille Dreyfus Teacher-Scholar Awards Program.

[1] A. Sharma and E. Ruckenstein, J. Colloid Interface Sci. **113**, 456 (1986).
[2] A. Oron, S. H. Davis, and S. G. Bankoff, Rev. Mod. Phys. **69**, 931 (1997).
[3] Y. O. Kabova, A. Alexeev, T. Gambaryan-Roisman, and P. Stephan, Phys. Fluids **18**, 012104 (2006).
[4] C. M. Gramlich, S. Kalliadasis, and G. M. Homsy, Phys. Fluids **14**, 1841 (2002).
[5] D. L. DeVoe, IEEE Trans. Compon. Packag. Technol. **25**, 576 (2003).
[6] A. A. Darhuber, J. M. Davis, S. M. Troian, and W. W. Reisner, Phys. Fluids **15**, 1295 (2003).
[7] A. A. Darhuber, J. P. Valentino, J. M. Davis, S. M. Troian, and S. Wagner, Appl. Phys. Lett. **82**, 657 (2003).
[8] J. Davies and E. Rideal, *Interfacial Phenomena* (Academic Press, New York, 1963).
[9] J. R. Pearson, J. Fluid Mech. **4**, 489 (1958).
[10] C. V. Sternling and L. E. Scriven, AIChE J. **5**, 514 (1959).
[11] S. H. Davis, Annu. Rev. Fluid Mech. **19**, 403 (1987).
[12] M. K. Smith and S. H. Davis, J. Fluid Mech. **134**, 119 (1983).
[13] M. K. Smith and S. H. Davis, J. Fluid Mech. **134**, 145 (1983).
[14] S. Joo, S. H. Davis, and S. Bankoff, J. Fluid Mech. **230**, 117 (1991).
[15] S. Joo, S. H. Davis, and S. Bankoff, J. Fluid Mech. **321**, 279 (1996).
[16] C. Ruyer-Quil, B. Scheid, S. Kalliadasis, M. G. Velarde, and

R. K. Zeytounian, J. Fluid Mech. **538**, 199 (2005).
[17] S. Kalliadasis, E. A. Demekhin, C. Ruyer-Quil, and M. G. Velarde, J. Fluid Mech. **492**, 303 (2003).
[18] B. Scheid, C. Ruyer-Quil, U. Thiele, O. A. Kabov, J. C. Legros, and P. Colinet, J. Fluid Mech. **527**, 303 (2005).
[19] E. Sultan, A. Boudaoud, and M. B. Amar, J. Fluid Mech. **543**, 183 (2005).
[20] O. A. Kabov, Heat Transfer Res. **27**, 221 (1996).
[21] O. A. Kabov, Thermophys. Aeromech. **5**, 547 (1998).
[22] A. M. Frank and O. A. Kabov, Phys. Fluids **18**, 032107 (2006).
[23] S. M. Troian, E. Herbolzehimer, S. A. Safran, and J. F. Joanny, Europhys. Lett. **10**, 25 (1989).
[24] J. M. Skotheim, U. Thiele, and B. Scheid, J. Fluid Mech. **475**, 1 (2003).
[25] S. Kalliadasis, A. Kiyashko, and E. A. Demekhin, J. Fluid Mech. **475**, 377 (2003).
[26] S. Kalliadasis and G. M. Homsy, J. Fluid Mech. **448**, 387 (2001).
[27] J. M. Davis and S. M. Troian, Phys. Fluids **17**, 072103 (2005).
[28] M. A. Spaid and G. M. Homsy, Phys. Fluids **9**, 823 (1996).
[29] S. Kalliadasis, C. Bielarz, and G. M. Homsy, Phys. Fluids **12**, 1889 (2000).
[30] D. V. Zaitsev, O. A. Kabov, and A. R. Evseev, Exp. Fluids **34**, 748 (2003).
[31] O. A. Kabov and E. A. Chinnov, Russ. J. Eng. Thermophys. **7**, 1 (1997).
[32] J. M. Davis and S. M. Troian, Phys. Fluids **15**, 1344 (2003).
[33] J. M. Davis, B. J. Fischer, and S. M. Troian, in *Interfacial Fluid Dynamics and Transport Processes*, Lecture Notes in Physics Vol. 628, edited by R. Narayanan (Springer-Verlag Heidelberg, New York, 2003), pp. 79–106.
[34] J. M. Davis and S. M. Troian, Phys. Rev. E **67**, 016308 (2003).
[35] J. M. Davis and S. M. Troian, Phys. Rev. E **70**, 046309 (2004).
[36] J. M. Davis, D. E. Kataoka, and S. M. Troian, Phys. Fluids **18**, 092101 (2006).
[37] R. O. Grigoriev, Phys. Fluids **15**, 1363 (2003).
[38] L. N. Trefethen, A. E. Trefethen, S. C. Reddy, and T. A. Driscoll, Science **261**, 578 (1993).
[39] B. F. Farrell and P. J. Ioannou, J. Atmos. Sci. **53**, 2025 (1996).
[40] G. H. Golub and C. F. V. Loan, *Matrix Computations*, 2nd ed. (Johns Hopkins University Press, Baltimore, MD, 1990).
[41] R. O. Grigoriev, Physica D **209**, 105 (2005).
[42] A. M. Frank, Phys. Fluids **18**, 078106 (2006).